Climate Dynamics manuscript No.
(will be inserted by the editor)

Role of stratiform heating on the organization of convection over the monsoon trough

R. S. Ajayamohan · Boualem Khouider · Andrew J. Majda · Qiang Deng

Received: date / Accepted: date

R. S. Ajayamohan
Center for Prototype Climate Modelling, New York University Abu Dhabi, P.O. Box 129188, Abu Dhabi, UAE
E-mail: Ajaya.Mohan@nyu.edu

Boualem Khouider
Department of Mathematics and Statistics, University of Victoria,
P.O. BOX 3045 STN CSC, Victoria, BC, Canada V8W 3P4
E-mail: khouider@math.uvic.ca

Andrew J. Majda
Department of Mathematics and Center for Atmosphere-Ocean Science, Courant Institute, New York University, 251 Mercer Street, New York, NY 10012 USA
Center for Prototype Climate Modelling, New York University Abu Dhabi, P.O. Box 129188, Abu Dhabi, UAE
E-mail: jonjon@cims.nyu.edu

Qiang Deng
Center for Prototype Climate Modelling, New York University Abu Dhabi, P.O. Box 129188, Abu Dhabi, UAE
E-mail: qd2@nyu.edu

Abstract It has been recently demonstrated that stratiform heating (SH) plays a critical role in the scale-selection of organized tropical convection, in an aquaplanet version of a coarse-resolution Atmospheric General Circulation Model coupled to a stochastic multicloud cumulus parameterization scheme. It has been established that, in the case of an equatorially centered warm pool sea-surface forcing, when the model is tuned to produce stronger and space and time extended stratiform anvils, it promotes planetary and intraseasonal Madden-Julian oscillation (MJO)-like organization while in the cases of weaker and short lived stratiform clouds, it leads to synoptic-scale convectively coupled Kelvin-like waves. This is partly due to the extent and strength of stratiform downdrafts that trigger cold pools in the model's atmospheric boundary layer and partly to the important role of tilted heating in the MJO dynamics. The study is extended here to the case of an asymmetric forcing by placing the warm pool forcing north of the equator mimicking the migration of the Intertropical Convergence Zone (ITCZ) during summer to understand the impact of changes in SH on the monsoon dynamics. Six sensitivity experiments were carried out to investigate the response of convection over the monsoon trough (MT) to changes in SH and the latitude of the warm pool center (10°N vs 15°N). It is shown here that the mean monsoon circulation and convection over the MT is sensitive to SH, in the same fashion as in the case of an equatorial warm pool; while strong SH drives planetary- and intraseasonal-scale organization of convection over the MT, weaker SH promotes synoptic-scale waves. More precisely, northeastward propagating monsoon intraseasonal oscillations (MISO) prevail when SH is strong while low pressure systems (LPS)-like disturbances characterize the MT variability when SH is weaker, especially when the warm pool is at 15°N. While the strength of the MT increases with the SH, its westward extent is inversely proportional to the SH, which is consistent with the prevalence of westward moving LPS in this regime. Only in the purely LPS regime do the background vorticity and zonal wind profiles over the MT are consistent with observations. This further demonstrates the importance for the global

climate models to produce the correct climatology in order to better simulate synoptic disturbances such as LPS.

Keywords SH · Organized convection · Stochastic parametrization · Monsoon trough · Monsoon Intraseasonal oscillation · Northward propagation · Low pressure systems

1 Introduction

The monsoon trough (MT) is a pronounced semipermanent low pressure zone extending from the Bay of Bengal and central Indian/Gangetic plains up to northwestern India (Krishnamurti and Surgi, 1987; Narasimha et al, 1997; Wang, 2006). The significance of the east-west oriented MT in regulating the active and break cycles of the monsoon and thereby the seasonal and interannual rainfall variability over the Indian subcontinent has been well documented (see Krishnamurthy and Ajayamohan, 2010, for example). Typically, during a break phase of monsoon the MT shifts towards the foothills of Himalayas (Ramamurthy, 1969; Krishnamurthy and Ajayamohan, 2010). During an active monsoon, copious rainfall over MT is associated with northwestward moving low pressure systems (LPS), also known as lows and depressions (Mooley, 1973; Sikka, 1977; Krishnamurthy and Ajayamohan, 2010). The LPS typically has a life cycle of about 3-6 days and a spatial scale of 1000-2000 km (Mooley, 1973; Krishnamurti et al, 1975).

The observational and dynamical features of MT and its role in regulating the monsoon weather and climate has been studied in detail (e.g. Krishnamurti et al, 1975, 1976; Krishnamurthy and Ajayamohan, 2010). However, one of the fundamental aspects of MT which has been overlooked by previous studies is the two-way interaction between convection and large-scale circulation associated with synoptic- and planetary-scale convective systems over the MT region. It may be noted that only limited observational evidence is available on the nature of cloud systems over the MT. Observations reveal that tropical convection involves a multicloud system primarily consisting of congestus, deep and stratiform clouds

(Johnson et al, 1999; Mapes et al, 2006). Abhik et al (2013) showed that a similar trimodal pattern of cloud structure prevails over the MT region, according to Tropical Rainfall Measuring Mission (TRMM) data. Most global climate models (GCMs) have difficulty in realistically resolving tropical convection (Lin et al, 2006; Kim et al, 2009; Hung et al, 2013; Sabeerali et al, 2013) and the associated synoptic and planetary-scale convectively coupled waves. Krishnamurti et al (2010) evaluated the performance of three different cumulus parameterization schemes in representing the three dimensional structure of vertical heating with respect to the TRMM heating profiles over the monsoon domain. They found that most cumulus parameterization schemes overestimate the amplitude of heating, whereas others carry lower values. The models with different cumulus schemes also exhibit large errors in the placement of the vertical level of maximum heating, leading to erroneous simulated large-scale response. This predicament arises due to the misrepresentation of the multi-scale character of organized convection in the cumulus parameterization schemes used in the climate models (Majda, 2007; Moncrieff, 2013).

The vertical structure of clouds and their role in organized convection is widely recognized and documented in both observations and modeling studies (For e.g. Johnson et al, 1999; Kiladis et al, 2005; Mapes et al, 2006; Khouider and Majda, 2006a, 2008; Khouider et al, 2010; Peters et al, 2013; Dorrestijn et al, 2015). As already mentioned, tropical convective systems involve three main cloud-types: cumulus congestus, deep convective towers and stratiform anvils. While congestus clouds warm the lower troposphere and cool the upper troposphere, stratiform clouds warm the upper troposphere and and cool the lower troposphere. In contrast, the deep convective clouds warm the entire troposphere. While tropospheric warming by the various cloud types comes from the process of condensation, both radiative cooling and detrainment at the cloud top are thought to contribute to the upper tropospheric cooling by congestus clouds. More importantly, the low tropospheric cooling associated with stratiform cloud types is due to the evaporation of stratiform rain which falls through a dry environment. Moreover, the associated stratiform heating (SH) induces a front-to-rear tilt in the heating profile which in turn plays a vital role in the dynamics of tropical intraseasonal oscillations like the Madden-Julian oscillations (MJO; Kiladis et al, 2005) and monsoon intraseasonal oscillations (MISO; Chattopadhyay et al, 2009). The significance of stratiform clouds in the propagation and maintenance of tropical intraseasonal oscillations is recognized in various studies (e.g. Houze Jr., 1997; Schumacher and Houze, 2003; Chattopadhyay et al, 2009). Few studies report that the prevailing stratiform updrafts forced by the vertical ascent of monsoon LPS are crucial for the strengthening and weakening of the MT (Houze Jr and Churchill, 1987; Houze et al, 2007). One of undetermined questions is the role of stratiform clouds in determining the organization of convection and synoptic-scale variability over the MT. This issue assumes significance as realistic representation of monsoon synoptic variability is crucial in simulating realistic rainfall over the MT at all time scales (Goswami et al, 2003; Ajayamohan et al, 2010; Krishnamurthy and Ajayamohan, 2010; Praveen et al, 2015).

In this study, we use a coarse-resolution aquaplanet atmospheric general circulation model (AGCM) with a stochastic cumulus scheme to assess the role of stratiform clouds in regulating the horizontal scale at which convection is organized over MT. Namely, we extend a recent study by Khouider et al (2010); Deng et al (2015b) to study the role of SH to simulate organized planetary scale convection along the equator (MJO), to the case of MT dynamics. The success of the stochastic multicloud model (SMCM) and its deterministic counterpart (MCM) in simulating the MJO, convectively coupled waves, and MT dynamics, when coupled to the coarse-resolution HOMME AGCM, is well established in earlier publications (Khouider et al, 2011; Ajayamohan et al, 2013, 2014; Deng et al, 2015a). The capability of the coarse-resolution aquaplanet HOMME-MCM model to simulate the MJO and convectively coupled waves with a zonally uniform sea-surface temperature (SST) forcing is established (Khouider et al, 2011). Ajayamohan et al

(2013) considered the case of a warm-pool-like SST forcing to study the role of circumnavigating dry Kelvin waves in initiating new MJO events over the Indian Ocean/Western Pacific warm pool. The latter work is extended in Ajayamohan et al (2014) to the case of monsoon dynamics by progressively moving the warm pool location to the north, mimicking the seasonal migration of the Tropical Convergence Zone (TCZ). In Ajayamohan et al (2014), the authors showed that the model depicts eastward and northward propagating intraseasonal disturbances resembling the observed monsoon intraseasonal oscillations, when the warm pool is at 10°N and mostly synoptic-scale westward moving wave patterns, consistent with the monsoon low pressure systems (LPS), when the warm pool is at 15°N. The SMCM was first coupled to the coarse resolution aquaplanet HOMME AGCM in Deng et al (2015a) for the case of a uniform SST forcing. The SMCM-HOMME model not only simulates well the MJO as in the deterministic case (Khouider et al, 2011) but also exhibits a more realistic MJO variability as it reproduces intermittent MJO events in terms of the variety of both dynamical structures and wavelengths.

The paper is organized as follows. In Section 2, we describe the modeling set up and experiments considered in this study, namely, by changing the key SH fraction parameter and varying the location of the warm pool center (WPC) between 10°N and 15°N. In Section 3, we report and analyze the results of these experiments. Namely, we present the main transitions between northward intraseasonal regimes and westward LPS regimes and their effect of the dynamical structure and topology of the MT. Finally, a concluding discussion is given in Section 4.

2 The numerical model and experiments setup

The SMCM-HOMME is implemented by coupling a stochastic multicloud model to the High-Order Methods Modelling Environment (HOMME) dynamical core as a cumulus parameterization scheme (Khouider et al, 2010; Deng et al, 2015a), in an aquaplanet mode (Khouider et al, 2011; Deng et al, 2015a). HOMME, developed by the National Center for Atmospheric Research (NCAR; Taylor et al, 1997; Nair et al, 2009; Mishra et al, 2011), is a spectral element Atmospheric General Circulation Model (AGCM) based on a cubed-sphere discretization, where the Earth is tiled with quasi-uniform quadrilateral elements, free from polar singularities (Dennis et al, 2005; Nair and Tufo, 2007). It is worthwhile noting that both the deterministic and the stochastic versions of the MCM exist and they are both implemented in HOMME. The implementation framework of the deterministic MCM-HOMME invoking the modes of atmospheric vertical structure are described in Khouider et al (2011). The implementation of the SMCM-HOMME, presented for the first time in Deng et al (2015a), follows a similar framework.

While the deterministic MCM is aimed at representing the bulk statistics of various cloud types, in terms of the associated heating profiles, as the background/large-scale conditions are changing, the SMCM mimics in addition the subgrid variability associated with cloud dynamics. As mentioned above, the (S)MCM parameterization is based on judiciously chosen prescribed heating profile basis functions that are associated with three cloud types: congestus, deep and stratiform, that characterize tropical convection, which in turn forces the first and second baroclinic modes of the vertical structure (Majda, 2003). The heating basis functions are truncated at roughly 200 hPa to avoid unphysical warming of the upper atmosphere. Also a mask limiting the effect of the (S)MCM on the dynamical core to the tropics, between 40°S and 40°N, is applied and the model relaxes smoothly to the prescribed state of rest climatology outside theses boundaries.

In the (S)MCM, mid-level moisture regulates the transition between congestus and deep convection regimes. Dry (moist) mid-troposphere favours congestus (deep) heating while SH is set to trail deep convection. In the deterministic MCM, congestus and deep convection heating rates, which are assumed to be proportional to some measure of convective instability such as convective available potential energy (CAPE), are modulated by a continuous switch function which depends on mid-tropospheric dryness, while SH is solved by an adjustment differential equation towards a fraction of deep convection, with a three hours adjustment time scale (Khouider and Majda, 2006b, 2008). The mathematics of the SMCM on the other hand are a bit more involved. Simply put, a certain number of congestus, deep, and stratiform "clouds" (or sites to be more precise) are allowed to coexist within a single GCM grid box in a probabilistic sense and transitions between cloudy and non-cloudy states and from one cloud type to the other occur randomly with transition probabilities that depend on the background/large-scale state, according to whether it is favourable to one "cloud state" or the other. When positive CAPE is present to sustain convection, as in the deterministic case, a dry middle tropospheric state yields congestus clouds with high probability while transitions from congestus and clear sky states to deep convection are favoured when the middle troposphere is moist. It is important to stress here that despite the level of details the SMCM depicts, the end result is a simple probabilistic (multi-species) birth-death process whose practical implementation involves very little to no computational overhead, unlike for example the cloud resolving convective parameterization approach (Khairoutdinov et al, 2005). This is achieved through the technique of coarse graining. A complete description and a thorough mathematical derivation of the SMCM, based on multi-type lattice interacting particles modeling, can be found in Khouider et al (2010) for the case where local interactions between cloud sites are neglected, while the case with local interactions is considered in Khouider (2014). For practical reasons, only the SMCM without local interactions (Khouider et al, 2010) is implemented in a GCM (aquaplanet HOMME) and used here and in Deng et al (2015a) and Deng et al (2015b).

In a nutshell, the SMCM is a Markov process with conditional transition rates (R_{kl}) as listed in Table 1. For example, the transition rates from both clear sky and congestus to deep convection increase with increased convective available potential energy (CAPE) and mid-tropospheric moistness. This allows a naturally progressive transition to deep convection as observed in nature and avoids the too soon release of instability and too soon firing of deep convection which plague traditional mass flux schemes (Lin et al, 2006). The transition rates are modulated by the transition time scales τ_{kl}, which are set to be dependent on the GCM grid resolution through the parameter τ_{grid} (Frenkel et al, 2012). The number of lattice sites, $n \times n$ is another key parameter of the SMCM. Here we use the conservative value of $n = 40$ and $\tau_{grid} = 2$. The sensitivity of the simulations to various parameters of the SMCM like τ_{kl}, τ_{grid} and n is extensively documented in previous publications (e.g. Frenkel et al, 2012; Deng et al, 2015a).

For the reader's convenience, the SMCM closure equations and parameters are listed in Table 2. We note that the parameter of interest in the present study is the stratiform fraction α_s. We recall that, the results of Deng et al (2015b), with an equatorial WPC, indicate that large α_s values yield MJO-like planetary-scale organized convective disturbances while smaller α_s values lead to convectively coupled Kelvin-like waves. Furthermore, it is demonstrated in Deng et al (2015b) that a similar behaviour is achieved if the time scale of transitions from stratiform to clear sky is varied instead. Moreover, similar sensitivity was observed with the parameter μ that appears in the downdraft equation, in front of the SH. The parameter μ controls the contribution of mid-tropospheric cooling, by stratiform rain evaporation, to downdrafts which in turn cool and dry the boundary layer. This mechanism is believed to drive cold pools and gravity currents which help (re)initiate convection in the immediate neighborhood thus leading to propagation and organization of convection, via the stratiform instability (Mapes, 2000; Majda and Shefter, 2001). According to Deng et al (2015b), the physical reason why SH affects the ability of tropical convective to form coherent structures (a.k.a organization) at planetary scale is behind both the associated tilted heating (Lappen and Schumacher, 2014) and the extent and strength of the induced cold pools in the boundary layer. Since this study is in essence, as already pointed out, an extension of the work in Deng et al (2015b) to the off-equatorially centered heating, i.e. monsoon conditions, only variations of the parameter α_s are considered. Moreover, as in Deng et al (2015b), the SMCM-HOMME simulations are carried out with a horizontal resolution equivalent to ∼167 km combined with 26 vertical levels and a time step of 30 seconds.

To mimic the Indian Ocean/western Pacific warm pool, the sea surface evaporative forcing is raised over 60°E-180°E using a half cosine function and follows a Gaussian shape in the meridional direction (see Figure 1). The centre of the Gaussian is a tunable parameter to allow flexibility in mimicking the seasonal migration of the ITCZ (Ajayamohan et al, 2014). In particular, we are interested in monsoon dynamics, i.e. the case when the maximum surface forcing is located off the equator. However, as demonstrated in Ajayamohan et al (2014), the results can vary considerably, according to whether the WPC is located at 10°N or 15°N. Northward and eastward propagating intraseasonal disturbances are observed in the 10°N case whilst the 15°N experiment is characterized mainly by westward propagating synoptic systems (Ajayamohan et al, 2014), consistent with the monsoon LPS observed in nature.

As summarized in Table 4, we consider six different experiments, by varying both the latitudinal location of the WPC and the stratiform fraction parameter α_s, following Deng et al (2015b) and Ajayamohan et al (2014). The location of WPC is varied between 10°N and 15°N to assess the effect of SH on both the poleward and westward propagation of convection over the MT. In each experiment, the SMCM-HOMME is run freely, as an initial value problem, for 2000 days. The initial data consists of a state of rest with the temperature and moisture background profiles set to the GARP-GATE sounding (Grabowski, 2002). Outputs are collected every six hours and the results of the last 1000 days are analyzed to avoid model spin-up.

3 Results

3.1 From monsoon intraseasonal oscillations to low pressure systems

In Figure 2, we plot the Hovmöller diagrams of the 850 hPa zonal wind anomalies (with respect to the time mean) and precipitation in the last 1000 days of simulation, for the six experiments listed in Table 4 (averaged over 0° to 10°N for EXP1,2,3 and 0° to 15°N for EXP4,5,6). As we can see from these plots, the changes in the SH fraction, α_s, from 0.5 to 0.25 and to 0.125, are accompanied with drastic changes in the scale and extent of the wave disturbances simulated by the HOMME-SMCM model. When the warm pool is centred at 10°N (Figure 2 a,b,c), with $\alpha_s = 0.5$, the model displays essentially thick patches of precipitation and streaks of wind disturbances, concentrated between 120°E and 180°E, to the east side of the WPC (cf. Fig. 1), that are either slowly moving eastward or standing, alternated by suppressed periods on the intraseasonal time scale of roughly 40 days. As α_s is decreased, the convective activity expands westward covering both sides of the warm pool (between 60°E and 180°E) and consists essentially of synoptic-scale disturbances with time scales of a few days. As confirmed by the spectrum power plots presented below, when $\alpha_s = 0.25$, the model produces a cohesive mixture of eastward and westward synoptic disturbances with an apparent domination of eastward waves while with $\alpha_s = 0.125$, the westward and eastward events are alternated by clear periods of suppressed convection. When the warm pool is moved to 15°N (Figure 2 d,e,f), the overall trend remains the same but the intraseasonal disturbances seen with $\alpha_s = 0.5$ become more confined and the westward moving synoptic-scale disturbances are more evident; they dominate at both $\alpha_s = 0.25$ and $\alpha_s = 0.125$, though it is much clearer in the later case.

These results are consistent with the ones obtained by Deng et al (2015b), with the HOMME-SMCM, when the WPC is at the equator; the strength and extent of SH (and implicitly stratiform downdrafts) is shown to play a pivotal role in the scale-selection process of organized convection, on planetary versus synoptic scales. When the parameters controlling the strength and extent of SH are decreased, the simulated wave disturbances transit from MJO-like waves to convectively coupled Kelvin waves (Deng et al, 2015b). However, to differentiate the new results, specific to monsoon conditions, we plot in Figure 3 the North-South Hovmöllers of 850 hPa zonal wind anomalies and precipitation rates, averaged between 130°E and 150°E. Before we dig any further, it is worthwhile recalling that when the (deterministic) HOMME-MCM is used with an off equatorial WPC, in Ajayamohan et al (2014), it produces coherent monsoon-like disturbances consisting of northward and eastward moving monsoon intraseasonal oscillations (MISO) and westward moving synoptic disturbances, a proxy for low pressure systems (Ajayamohan et al, 2010). It is found in particular that when the WPC is at 10°N, MISO-like events dominate but when the WPC is at 15°N, the northward propagation ceases and synoptic-scale westward LPS-like systems become abundant (Ajayamohan et al, 2014). Consistently, we can see from the six panels of Figure 3 that the northward propagation coincides with the eastward intraseasonal disturbances obtained with $\alpha_s = 0.5$, in both 10°N and 15°N cases. The other cases, with weaker stratiform fractions, all leading to synoptic-scale disturbances, appear to have a more or less balanced north-south movement, which also appears to occur on shorter time scales. This is in fact confirmed by the spectral power plots reported in Figures 4 and 5.

From the top panels of Figures 4 and 5, we can see that the two cases with $\alpha_s = 0.5$ (Panels a) exhibit strong (and sharp) low frequency peaks, around 40 days, indicating eastward propagation of planetary-scale disturbances consistent with observations Suhas et al (2013). Consistently, the corresponding two bottom panels (d) show significant peaks on the bottom left of the plot, indicating northward propagation. With smaller α_s values the spectrum power distribution changes significantly. In terms of east-west movement, the two cases corresponding to a 10°N WPC (Figure 4 b, c), have both eastward and westward signals. The same applies, to some extent, to the case with a 15°N WPC and $\alpha_s = 0.25$. Before moving further to one of our most interesting results, we stress out that the eastward power peaks on panels (b) and (c) of Figure 4 and that on Figure 5 (b) are more or less aligned according to the dispersion-less dispersion relation curves of Kelvin waves, consistent with the results of Deng et al (2015b), while the westward signals suggest low pressure systems or depression-type disturbances

(Wheeler and Kiladis, 1999). In the corresponding north-south plots, i.e. Figure 4 (e,f) and Figure 5(e), both northward and southward tendencies are consistent with the associated Hovmöller diagrams in Figure 3 (b,c,e). Interestingly, with both the WPC at 15°N and $\alpha_s = 0.125$, HOMME-SMCM yields mainly westward moving disturbances, which we qualify as low pressure systems. The structural resemblance of these disturbances to observed LPS, thus the justification for this denomination, is confirmed below in Section 3.3.

3.2 Mean flow and variability of monsoon trough structure

In Figures 6 and 7, we represent the time mean solution, averaged over the last 1000 days, for each one of the six experiments listed in Table 4. Specifically, we plot the 850 hPa horizontal wind vectors and the shaded contours of relative vorticity (a,c,e), while the latitude-height mean circulation (local Hadley cell) is depicted by the associated mean wind vectors and contours of heating (b,d,f). Except for a few noticeable details, which will be discussed later, the two sets of pictures exhibit some very important common bulk features.

On the left panels we can see that all six experiments seem to capture a well defined mean monsoon flow structure near the surface, centred around the warm pool longitude, indicated by a dashed line. It is characterized by easterlies on and at slightly south of the equator, surmounted by westerlies extending around 10°N. The two are connected by a northerly flow at the eastern edge of the warm pool (resembling the Somali jet). The region between 10°N and 20°N is characterized by an extended patch of positive vorticity consistent with the MT (Goswami and Ajayamohan, 2001; Trenberth et al, 2006; Sultan et al, 2003). Also, the flow on the right panels is characterized by overall rising air in the Northern Hemisphere and subsiding in the Southern Hemisphere, consistent with the local Hadley circulation, during the summer monsoon season. However, both flow views exhibit quite interesting differences throughout the six experiments.

On the left panels, we can see, for example, that, as α_s is decreased from 0.5 to 0.125, the MT smoothly shrinks equatorward and at the same time it expands westward. This is consistent with the persistence (absence) of northward propagating MISO-like signals when $\alpha_s = 0.5$ ($\alpha_s = 0.25, 0.125$) and the persistence (absence) of westward propagating LPS-like disturbance when $\alpha_s = 0.25, 0.125$ ($\alpha_s = 0.5$); the northward propagating MISO's "carry" low-level positive vorticity northward while westward moving LPS's "carry" low-level positive vorticity westward. These differences seem to be more pronounced in the 15°N cases.

From the right panels, in both WPC locations, the flow structure is mostly second baroclinic for the two larger α_s values (0.5 and 0.25) and transits to a first baroclinic one at $\alpha_s = 0.125$. With $\alpha_s = 0.5$ or 0.25, the circulation consists of two cells, one on top of the other. The upper cell rises in the north of the equator and sinks in the south while the lower cell, also significantly weaker, rises in the south of the equator and sinks in the north. Consistently, the heating fields exhibit upper tropospheric warming and lower tropospheric cooling in the Northern Hemisphere suggesting the dominance of stratiform clouds there while the Southern Hemisphere is characterized by lower troposphere warming and upper tropospheric cooling, which is the main characteristic of congestus clouds. On the bottom panels (f), consistent with the first baroclinic structure, we have a (perhaps more physical) single cell that rises in the Northern Hemisphere and sinks south of the equator. The associated heating field is characterized by mid-tropospheric warming in the north, an indication of a deep convection dominated regime, and cooling of the mid-to-upper troposphere in the south of the equator suggesting the persistence of congestus clouds there.

In Figure 8, we depict the horizontal distribution of mean and variance of the precipitation rate for the experiments 4,5,6 corresponding to the cases with a WPC at 15°N. The 10°N cases are fairly similar so they are not repeated here. As we can see, similar to the drastic changes observed in the wave activity and mean flow structure, the distribution of precipitation mean and variance follows consistent transitional behaviour both in terms of their relative strength and zonal extent. In the $\alpha_s = 0.5$ regime, 1) the precipitation mean and variance are fairly confined to the eastern side of the warm pool, around 160°E, and between roughly 10°N and 25°N and 2) the variance appears to be much stronger than the mean. In the weaker stratiform cases ($\alpha_s = 0.25, 0.125$), however, 1) the mean and variance shift slightly toward the equator and at the same time extend westward to cover both sides of the warm pool and 2) the relative strengths of the mean and variance smoothly transit and reverse the tendency to exhibit at $\alpha_s = 0.125$ a stronger mean and weaker variance. Just like the trough structure, the westward and northward extension of the precipitation mean and variance, and their lack thereof, are associated with the presence or not of the northward movement of MISO-like systems and the westward propagation of LPS-like features, respectively.

The transition in strength of mean and variance is a new feature which deserves some close attention. It is tempting to argue that the decrease of the variance with decreasing α_s can be explained by the law of large numbers because there are more synoptic events in 1000 days run than the intraseasonal ones. But a closer look at the Hovmöller diagrams in Figure 2, for example, reveals that the middle case ($\alpha_s = 0.25$) appears to have way more synoptic events than the bottom one ($\alpha_s = 0.125$). In fact, the decrease in variance and increase in mean, are two intriguing features that cannot be explained by the sole presence of synoptic versus intraseasonal disturbance. It is not clear whether this has any physical meaning at all. Unfortunately, we have a single earth system and we cannot easily separate the presence of synoptic versus intraseasonal disturbances in observation data, for comparison.

3.3 Monsoon trough depth, background shear and vertical structure of low pressure systems

In Figure 9, we plot horizontal slices of the flow velocity (arrows) and vertical vorticity (shading) at 700 hPa, 400 hPa and 200 hPa, for the three experiments with the WPC at 15°N. One common feature of all these experiments is the inherent baroclinic structure of the wind field in the vicinity of the trough, especially the return flow, which characterizes the cross equatorial jet; north-westerlies near the surface are overlaid by south-easterlies aloft. For the two cases with smaller stratiform fractions, $\alpha_s = 0.25$ and 0.125 (EXP5 and EXP6), this is accompanied with a trough vorticity reversal. But in the first case, with $\alpha_s = 0.5$ (EXP4), the corresponding patch of positive vorticity extents to the upper troposphere, although, at 200 hPa, it becomes weaker and much narrower. Also, for $\alpha_s = 0.25$, the vorticity reversal occurs above 400 hPa while for $\alpha_s = 0.125$, it occurs below this level. As suggested by previous studies (e.g. Praveen et al, 2015), the depth of MT (i.e. positive vorticity) and the level of its reversal thereof may have some cause and/or effect relationship with the persistence or not of LPS-disturbances.

To dig a little further into this issue, we present in Figure 10 the vertical profiles of the zonal wind and relative vertical vorticity, averaged in time over the last 1000 days and horizontally over the box 10°N–20°N and 80°E–180°E, for EXP4,5,6, compared against the European Centre for Medium Range Weather Forecast (ECMWF) reanalysis data (ERAI; Dee et al, 2011). We notice that all three cases present qualitatively similar features as the reanalysis data in terms of both the zonal wind and vorticity profiles. They more or less all present westerlies near the surface capped by easterlies aloft and positive vorticity below negative vorticity. However, there are significant differences regarding the level at which both the zonal wind and vorticity change signs. In terms of zonal winds, the $\alpha_s = 0.5$ and $\alpha_s = 0.25$ cases predict strong westerlies in the mid-troposphere while both the ERAI and the $\alpha_s = 0.125$ cases suggest easterlies at those levels. Similarly, consistent with the horizontal slices in Fig. 9, positive vorticity extends to almost 200 hPa for the first two cases, while in both ERAI and the $\alpha_s = 0.125$ case the vorticity reversal occurs at roughly the same level, around 600 hPa. Though the vorticity magnitude at both low and upper levels is somewhat stronger in the $\alpha_s = 0.125$ case compared to ERAI, the corresponding zonal wind profiles seem to match fairly well, at least below the 200 hPa mark which delimits the penetration of the prescribed heating basis functions (i.e. no convective heating is applied above this level). The proximity of the zonal wind and vorticity profiles to the reanalysis data explains in part why the $\alpha_s = 0.125$ case is the most successful in producing LPS-like disturbances since LPS exist in nature, over the MT, under these conditions (i.e. the ERAI zonal wind and vorticity profiles Krishnamurthy and Ajayamohan, 2010; Goswami et al, 1980; Xavier and Joseph, 2000). This finding is inline with the results of Praveen et al (2015) who demonstrated that the ability of GCMs to simulate LPS is highly correlated with their ability to have a good representation of the background climatology, the vertical shear in particular.

On the left panel of Figure 11, we reproduce a closeup of the Hovmöller diagram of precipitation for EXP6 (WPC at 15°N and $\alpha_s = 0.125$). This showcases the persistence of westward synoptic disturbances reminiscent to low pressure systems (Goswami et al, 1980, 2003). The dashed lines mark a reference speed of about 20 m s^{-1} consistent with their synoptic-scale character. On the right panels, we display the composite vertical structure for the two events indicated by the blue and red circles on the left panel. Consistent with observations of LPS (Mooley and Shukla, 1989, 1987; Hurley and Boos, 2015; Praveen et al, 2015), the disturbances pictured in Figure 11 (b,c) are characterized by warm temperature anomalies in the upper troposphere overlying cold anomalies near the surface and nearly barotropic wind structure. A jump in cross equatorial flow coincides with the active center of the wave, defined by the negative temperature anomaly near the surface (low pressure), and extends vertically up to 300 hPa. It is topped by a strong vertical jump in the cross equatorial flow. Southerlies (northerlies) prevailing to the east (west) of the wave center implies a significant anomalous cyclonic vorticity carried by the waves; an indication that these LPS-like structures potentially reinforce the MT as suggested in earlier studies (Krishnamurthy and Ajayamohan, 2010). It is important to note that, with such a coarse resolution of $\sim$167 km used here, synoptic systems (such as Kelvin waves and LPS) are only marginally resolved, yet the structure of the simulated LPS-like disturbances presented in Fig. 11 (b,c) are impressively realistic (Krishnamurthy and Ajayamohan, 2010).

4 Conclusion

This study examines the role of SH in the dynamics and variability of the monsoon flow. We use the NCAR HOMME AGCM, at coarse resolution, coupled to the stochastic multicloud model (Khouider et al, 2011, 2010; Deng et al, 2015a,b). We conducted a series of numerical simulations with a fixed WPC at two different locations, 10°N and 15°N (Ajayamohan et al, 2014). The warm pool is designed to represent the observed SST structure in the Indo-West Pacific ocean and the northward movement of the ITCZ during the summer monsoon season (Ajayamohan et al, 2014). We extended the work of Deng et al (2015b), conducted in the case of a WPC at the equator, to the monsoon environment. It is shown in Deng et al (2015b) that the planetary-scale organization of convection in the coupled HOMME-SMCM model, in terms of MJO-like vs. Kelvin wave disturbances, is mainly controlled by the strength and temporal and spatial extent of SH. As argued in Deng et al (2015b), the reason behind this behaviour is twofold. Firstly, the SH induces a significant tilt in the heating profile, which is believed to be important for organized convection and the MJO in particular (Moncrieff, 1981; Houze Jr., 1997; Schumacher and Houze, 2003; Khouider et al, 2011; Lappen and Schumacher, 2014). Secondly, the multicloud parameterization takes into account the evaporation of stratiform rain in the lower troposphere and its capacity to generate downdrafts that in turn trigger cold pools in the boundary layer, which are believed to be important for the propagation and organization of convection (Mapes, 1993; Houze Jr., 1997; Moncrieff, 2004; Stechmann and Majda, 2009; Feng et al, 2015; Moncrieff, 2013). The importance of SH to drive the second baroclinic mode and trigger convectively coupled gravity waves through the stratiform instability is established in a few studies (Mapes, 2000; Majda and Shefter, 2001). The key specific role played by stratiform downdrafts is demonstrated in Majda et al (2004).

In the SMCM, the strength and extent of SH can be controlled by various parameter combinations. In particular, the stratiform fraction parameter (α_s) and the transition time scale of stratiform clouds to clear sky (τ_{30}) are found to be very effective in this regard (Deng et al, 2015b). For the sake of simplicity, here we only considered variations in the stratiform fraction parameter, α_s. The three values $\alpha_s = 0.5, 0.25, 0.125$ were considered and the simulation results were thoroughly compared and analyzed. Accordingly, six sensitivity experiments (Table 4) were conducted, by combining the three α_s values with the two WPC locations.

Consistent with the findings of Deng et al (2015b), it is established here that the simulations with stronger stratiform area fraction ($\alpha_s = 0.5$, EXP1 and EXP4) result in MISO-like intraseasonal disturbances, exhibiting both northward and eastward propagation while the simulations with smaller α_s (i.e. all the other experiments) result in a mixture of eastward and westward synoptic-scale waves. The synoptic disturbances mimic somehow the prevalence of both Kelvin waves and monsoon-like LPS, except perhaps for the one case with $\alpha_s = 0.125$ and WPC at 15°N (EXP6) where LPS-like disturbances are found to dominate. If this is to be contrasted with the case with the WPC at the equator, studied in Deng et al (2015b), the MISO disturbances replace the MJO while LPS take the place of Kelvin waves. This enforces the results of Deng et al (2015b) who concluded that the organization of convection at planetary scales requires a significant SH proportion.

Furthermore, it is shown here that, at least for EXP6, the LPS-like westward propagating convective systems that are simulated in the case of low stratiform fraction share many common features with observed LPS (Krishnamurthy and Ajayamohan, 2010), including cold temperatures underlying warm temperatures in the region of cyclonic vorticity, which defines the wave center, despite the coarse resolution of ∼167 km employed by the HOMME-SMCM model. This, in particular, evidences the importance of the stochasticity in climate models and the overall design principle of the SMCM, which is aimed to represent the missing intermittent variability associated with organized tropical convection as well as the underlying physical mechanisms of organized convection that lead to large-scale coherent structures (at the mesoscale and beyond), such as the built-in cloud-cloud interactions and the (stochastic) interactions between clouds and the environmental moisture. These results insinuate the need for including stratiform rain in parameterization schemes to better simulate MISO and monsoon LPS (sic the MJO and convectively coupled Kelvin waves). It may be noted that the state-of-the-art GCMs have difficulty in simulating monsoon LPS (Praveen et al, 2015). Since 60% of rainfall over the MT is caused by LPS (Praveen et al, 2015), accurately simulating the structure and amplitude of LPS assumes significance.

This extreme sensitivity of the scale-selective organization, of tropical convection, to SH is probably the root cause for underestimation of cumulus convection in climate models. In nature and to some extent in climate models, the strength of SH is dictated by large-scale environmental parameters. However, although stratiform rain is dependent on deep convection, their relationship cannot be a linear one as suggested by the use of a fixed stratiform fraction parameter to assign the strength of SH. This study suggests an urgent need for new methods to represent stratiform rain in climate models.

Acknowledgements

The Center for Prototype Climate Modelling (CPCM) is fully funded by the Abu Dhabi Government through New York University Abu Dhabi (NYUAD) Research Institute grant. This research was initiated during an extended visit of BK and AM to the CPCM at NYUAD during winter 2014. The computations were carried out on the High Performance Computing resources at NYUAD and early tuning of the code were done at the University of Victoria using the West Grid computing Network. The research of AM is partially supported by the Office of Naval Research

Grant ONR MURI N00014-12-1-0912. The research of BK is partially funded by Monsoon Mission Project, MoES, Government of India.

References

Abhik S, Halder M, Mukhopadhyay P, Jiang X, Goswami BN (2013) A possible new mechanism for northward propagation of boreal summer intraseasonal oscillations based on TRMM and MERRA reanalysis. Clim Dynam 40(7-8):1611–1624, DOI 10.1007/s00382-012-1425-x

Ajayamohan RS, Merryfield WJ, Kharin VV (2010) Increasing trend of synoptic activity and its relationship with extreme rain events over central India. J Climate 23(4):1004–1013, DOI 10.1175/2009JCLI2918.1

Ajayamohan RS, Khouider B, Majda AJ (2013) Realistic initiation and dynamics of the Madden-Julian Oscillation in a coarse resolution GCM. Geophys Res Lett 40, DOI 10.1002/2013GL058187

Ajayamohan RS, Khouider B, Majda AJ (2014) Simulation of monsoon intraseasonal oscillations in a coarse-resolution aquaplanet GCM. Geophys Res Lett 41, DOI 10.1002/2014GL060662

Chattopadhyay R, Goswami BN, Sahai A, Fraedrich K (2009) Role of stratiform rainfall in modifying the northward propagation of monsoon intraseasonal oscillation. J Geophys Res 114(D19), DOI 10.1029/2009JD011869

Dee DP, Uppala SM, Simmons AJ, Berrisford P, Poli P, Kobayashi S, Andrae U, Balmaseda MA, Balsamo G, Bauer P, Bechtold P, Beljaars ACM, van de Berg L, Bidlot J, Bormann N, Delsol C, Dragani R, Fuentes M, Geer AJ, Haimberger L, Healy SB, Hersbach H, Hlm EV, Isaksen L, Kllberg P, Khler M, Matricardi M, McNally AP, Monge-Sanz BM, Morcrette JJ, Park BK, Peubey C, de Rosnay P, Tavolato C, Thpaut JN, Vitart F (2011) The era-interim reanalysis: configuration and performance of the data assimilation system. Quarterly Journal of the Royal Meteorological Society 137(656):553–597, DOI 10.1002/qj.828

Deng Q, Khouider B, Majda A (2015a) The MJO in a coarse-resolution GCM with a stochastic multicloud parameterization. J Atmos Sci 72:55–74, DOI 10.1175/JAS-D-14-0120.1

Deng Q, Khouider B, Majda A, Ajayamohan R. S. (2015b) Effect of stratiform heating on the planetary-scale organization of tropical convection. J Atmos Sci Submitted

Dennis J, Fournier A, Spotz WF, St-Cyr A, Taylor MA, Thomas SJ, Tufo HM (2005) High-resolution mesh convergence properties and parallel efficiency of a spectral element atmospheric dynamical core. International Journal of High Performance Computing Applications 19(3):225–235, DOI 10.1177/1094342005056108

Dorrestijn J, Crommelin DT, Siebesma AP, Jonker HJJ, Jakob C (2015) Stochastic parameterization of convective area fractions with a multicloud model inferred from observational data. J Atmos Sci 72:854–869

Feng Z, Hagos S, Rowe AK, Burleyson CD, Martini MN, de Szoeke SP (2015) Mechanisms of convective cloud organization by cold pools over tropical warm ocean during the AMIE/DYNAMO field campaign. J Adv Model Earth Syst 07:1–25, DOI 10.1002/2014MS000384

Frenkel Y, Majda AJ, Khouider B (2012) Using the stochastic multicloud model to improve tropical convective parameterization: A paradigm example. J Atmos Sci 69:1080–1105, DOI 10.1175/JAS-D-11-0148.1

Goswami BN, Ajayamohan RS (2001) Intraseasonal oscillations and interannual variability of the Indian summer monsoon. J Climate 14:1180–1198, DOI 10.1175/1520-0442(2001)014¡1180:IOAIVO¿2.0.CO;2

Goswami BN, Keshavamurthy RN, Satyan V (1980) Role of barotropic, baroclinic and combined barotropic-baroclinic instability for the growth of monsoon depressions and mid-tropospheric cyclones. Proc India Acad Sci (Earth Planet Sci) 89:79–97, DOI 10.1007/BF02841521

Goswami BN, Ajayamohan RS, Xavier PK, Sengupta D (2003) Clustering of low pressure systems during the Indian summer monsoon by intraseasonal oscillations. Geophys Res Lett 30:1431, DOI 10.1029/20002GL016734

Grabowski WW (2002) Large-scale organization of moist convection in idealized aquaplanet simulations. Int J Numer Methods Fluids 39:843–853

Houze RA, Wilton DC, Smull BF (2007) Monsoon convection in the himalayan region as seen by the trmm precipitation radar. Quart J Roy Meteorol Soc 133(627):1389–1411, DOI 10.1002/qj.106

Houze Jr RA (1997) Stratiform precipitation in regions of convection: A meteorological paradox? Bull Amer Meteor Soc 78:2179–2196

Houze Jr RA, Churchill DD (1987) Mesoscale organization and cloud microphysics in a bay of bengal depression. J Atmos Sci 44(14):1845–1868

Hung MP, Lin JL, Wang W, Kim D, Shinoda T, Weaver SJ (2013) Mjo and convectively coupled equatorial waves simulated by cmip5 climate models. J Climate 26(17):6185–6214, DOI 10.1175/JCLI-D-12-00541.1

Hurley JV, Boos WR (2015) A global climatology of monsoon low pressure systems. Quart J Roy Meteorol Soc 141:1049–1064, DOI 10.1002/qj.2447

Johnson RH, Rickenbach TM, Rutledge SA, Ciesielski PE, Schubert WH (1999) Trimodal characteristics of tropical convection. J Climate 12(8):2397–2418

Khairoutdinov M, Randall D, Demott C (2005) Simulations of the atmospheric general circulation using a cloud-resolving model as a superparameterization of physical processes. J Atmos Sci 62:2136–2154

Khouider B (2014) A coarse grained stochastic multi-type particle interacting model for tropical convection: nearest neighbour interactions. Comm Math Sci 12(8):1379–1407, DOI 10.4310/CMS.2014.v12.n8.a1

Khouider B, Majda AJ (2006a) Model multi-cloud parameterizations for convectively coupled tropical waves: Detailed nonlinear wave evolution. Dynam Atmos Oceans 42:59–80

Khouider B, Majda AJ (2006b) A simple multicloud parameterization for convectively coupled tropical waves. Part I: Linear analysis. J Atmos Sci 63:1308–1323

Khouider B, Majda AJ (2008) Multicloud model for organized tropical convection: Enhanced congestus heating. J Atmos Sci 65:895–914

Khouider B, Biello J, Majda AJ, et al (2010) A stochastic multicloud model for tropical convection. Comm Math Sci 8(1):187–216

Khouider B, St-Cyr A, Majda AJ, Tribbia J (2011) The MJO and convectively coupled waves in a coarse resolution GCM with a simple multicloud parameterization. J Atmos Sci 68:240–264, DOI 101.1175/2010JAS3443.1

Kiladis GN, Straub K, Haertel P (2005) Zonal and vertical structure of the Madden-Julian oscillation. J Atmos Sci 62:2790–2809, DOI 10.1175/JAS3520.1

Kim D, Sperber K, Stern W, Waliser D, Kang IS, Maloney E, Wang W, Weickmann K, Benedict J, Khairoutdinov M, Lee MI, Neale R, Suarez M, Thayer-Calder K, Zhang G (2009) Application of MJO simulation diagnostics to climate models. J Climate 22(23):6413–6436, DOI 10.1175/2009JCLI3063.1

Krishnamurthy V, Ajayamohan RS (2010) Composite structure of monsoon low pressure systems and its relation to Indian rainfall. J Climate 23(16):4825–4305, DOI 10.1175/2010JCLI2953.1

Krishnamurti T, Surgi N (1987) Observational aspects of summer monsoon. In: Chang CP, Krishnamurti TN (eds) Monsoon Meteorology, 7, Oxford University Press, NY, pp 3–25

Krishnamurti TN, Kanamitsu M, Godbole R, Chang CB, Carr F, Chow JH (1975) Study of a monsoon depression (i): Synoptic structure. J Meteorol Soc Japan 53:227–239

Krishnamurti TN, Kanamitsu M, Godbole R, Chang CB, Carr F, Chow JH (1976) Study of a monsoon depression (ii): Dynamical structure. J Meteorol Soc Japan 54:208–224

Krishnamurti TN, Chakraborty A, Mishra AK (2010) Improving multimodel forecasts of the vertical distribution of heating using the trmm profiles. J Climate

23(5):1079–1094, DOI 10.1175/2009JCLI2878.1

Lappen CL, Schumacher C (2014) The role of tilted heating in the evolution of the MJO. J Geophys Res Atmos 119:2966–2989

Lin JL, Kiladis GN, Mapes BE, Weickmann KM, Sperber KR, W Lin MCW, Schubert SD, Genio AD, donner LJ, Emori S, Gueremy JF, Hourdin F, Rasch PJ, Roeckner E, Scinocca JF (2006) Tropical intraseasonal variability in 14 IPCC AR4 climate models Part I: Convective signals. J Climate 19:2665–2690

Majda AJ (2003) Introduction to PDEs and Waves for the Atmosphere and Ocean, Courant Lecture Notes in Mathematics, vol 9. American Mathematical Society, Providence

Majda AJ (2007) New multiscale models and self-similarity in tropical convection. J Atmos Sci 64(4):1393–1404, DOI 10.1175/JAS3880.1

Majda AJ, Shefter M (2001) Models for stratiform instability and convectively coupled waves. J Atmos Sci 58:1567–1584

Majda AJ, Khouider B, Kiladis GN, Straub KH, Shefter MG (2004) A model for convectively coupled tropical waves: Nonlinearity, rotation, and comparison with observations. J Atmos Sci 61:2188–2205

Mapes B, Tulich S, Lin J, Zuidema P (2006) The mesoscale convection life cycle: Building block or prototype for large-scale tropical waves? Dynam Atmos Oceans 42:3–29, DOI 10.1016/dynatmoce.2006.03.003

Mapes BE (1993) Gregarious tropical convection. J Atmos Sci 50:2026–2037

Mapes BE (2000) Convective inhibition, subgrid-scale triggering energy, and stratiform instability in a toy tropical wave model. J Atmos Sci 57(10):1515–1535

Mishra SK, Taylor MA, Nair RD, Lauritzen PH, Tufo HM, Tribbia JJ (2011) Evaluation of the homme dynamical core in the aquaplanet configuration of ncar cam4: Rainfall. J Climate 24(15):4037–4055, DOI 10.1175/2011JCLI3860.1

Moncrieff M (1981) A theory of organized steady convection and its transport properties. Quart J Roy Meteorol Soc 107(451):29–50, DOI 10.1002/qj.49710745103

Moncrieff MW (2004) Analytic representation of the large-scale organization of tropical convection. J Atmos Sci 61(13):1521–1538, DOI 10.1175/1520-0469(2004)061¡1521:AROTLO¿2.0.CO;2

Moncrieff MW (2013) The multiscale organization of moist convection and the intersection of weather and climate. In: Sun DZ, Bryan F (eds) Climate Dynamics: Why Does Climate Vary?, American Geophysical Union, pp 3–26, DOI 10.1029/2008GM000838

Mooley DA (1973) Some aspects of Indian monsoon depressions and the associated rainfall. Mon Weather Rev 101:271–280

Mooley DA, Shukla J (1987) Characteristics of the westward moving summer monsoon low pressure systems over the Indian region and their relationship with the monsoon rainfall. Center for Ocean Land Atmosphere Studies, Calverton, MD 20705, USA, available from COLA, USA

Mooley DA, Shukla J (1989) Main features of the westward-moving low pressure systems which form over the Indian region during the summer monsoon season and their relation to the monsoon rainfall. Mausam 40:137–152

Nair R, Tufo HM (2007) Petascale atmospheric general circulation models. In: Journal of Physics: Conference Series, IOP Publishing, vol 78, p 012078, DOI doi:10.1088/1742-6596/78/1/012078

Nair RD, Choi HW, Tufo H (2009) Computational aspects of a scalable high-order discontinuous galerkin atmospheric dynamical core. Computers & Fluids 38(2):309–319, DOI 10.1016/j.compfluid.2008.04.006

Narasimha R, Sikka D, Prabhu A (1997) The monsoon trough boundary layer. Indian Academy of Sciences, Bangalore p 422 pp

Peters K, Jakob C, Davies L, Khouider B, Majda AJ (2013) Stochastic behavior of tropical convection in observations and a multicloud model. J Atmos Sci 70:3556–3575, DOI doi: http://dx.doi.org/10.1175/JAS-D-13-031.1

Praveen V, Sandeep S, Ajayamohan RS (2015) On the relationship between mean monsoon precipitation and low pressure systems in climate model simulation. J

Climate in press, DOI 10.1175/2010JCLI2953.1

Ramamurthy K (1969) Monsoon of India: Some aspects of 'break' in the Indian south west monsoon during July and August. Tech. rep., India Meteorological Department, New Delhi, forecasting Manual, Part IV.18.3

Sabeerali C, Ramu Dandi A, Dhakate A, Salunke K, Mahapatra S, Rao SA (2013) Simulation of boreal summer intraseasonal oscillations in the latest CMIP5 coupled GCMs. J Geophys Res 118(10):4401–4420, DOI 10.1002/jgrd.50403

Schumacher C, Houze RAJ (2003) Stratiform rain in the tropics as seen by the TRMM precipitation radar. J Climate 16

Sikka DR (1977) Some aspects of the life history, structure and movement of monsoon depressions. Pure Appl Geophys 115:1501–1529

Stechmann SN, Majda AJ (2009) Gravity waves in shear and implications for organized convection. J Atmos Sci 66:2579–2599

Suhas E, Neena J, Goswami BN (2013) An indian monsoon intraseasonal oscillations (miso) index for real time monitoring and forecast verification. Clim Dynam 40(11-12):2605–2616, DOI 10.1007/s00382-012-1462-5

Sultan B, Janicot S, , Diedhiou A (2003) The west african monsoon dynamics. part i: Documentation of intraseasonal variability. J Climate 16:3389–3406

Taylor M, Tribbia J, Iskandarani M (1997) The spectral element method for the shallow water equations on the sphere. Journal of Computational Physics 130(1):92–108, DOI 10.1006/jcph.1996.5554

Trenberth KE, Hurrell JW, Stepaniak DP (2006) The Asian monsoon: Global perspectives. In: Wang B (ed) The Asian Monsoon, 1st edn, Springer, Heidelberg, Germany, chap 2, pp 67–87

Wang B (ed) (2006) The Asian Monsoon, 1st edn. Springer, Heidelberg, Germany

Wheeler M, Kiladis GN (1999) Convectively coupled equatorial waves: Analysis of clouds and temperature in the wavenumber-frequency domain. J Atmos Sci 56:374–399

Xavier PK, Joseph PV (2000) Vertical wind shear in relation to frequency of monsoon depressions and tropical cyclones of Indian seas. In: Proceedings of TROPMET-2000, Kochi, India, pp 242–245

Table 1 Transition rates and time scales in the stochastic parameterization.

Transition	Transition Rate	Time scale (h)
Formation of congestus	$R_{01} = \frac{1}{\tau_{01}} \Gamma(C_l)\Gamma(D)$	$\tau_{01} = 40\tau_{grid}$
Decay of congestus	$R_{10} = \frac{1}{\tau_{10}} \Gamma(D)$	$\tau_{10} = 1\tau_{grid}$
Conversion of congestus to deep	$R_{12} = \frac{1}{\tau_{12}} \Gamma(C)[1 - \Gamma(D)]$	$\tau_{12} = 1\tau_{grid}$
Formation of deep	$R_{02} = \frac{1}{\tau_{02}} \Gamma(C)[1 - \Gamma(D)]$	$\tau_{02} = 4\tau_{grid}$
Conversion of deep to stratiform	$R_{23} = \frac{1}{\tau_{23}}$	$\tau_{23} = 3\tau_{grid}$
Decay of deep	$R_{20} = \frac{1}{\tau_{20}} [1 - \Gamma(C)]$	$\tau_{20} = 3\tau_{grid}$
Decay of stratiform	$R_{30} = \frac{1}{\tau_{30}}$	$\tau_{30} = 5\tau_{grid}$
$\Gamma(x) = \begin{cases} 1 - \exp(-x), \text{ if } x > 0; \\ 0, \qquad\qquad \text{otherwise.} \end{cases}$	$D = (\theta_{eb} - \theta_{em})/T_0$	
$CAPE_l = \overline{CAPE} + R[\theta_{eb} - \gamma(\theta_1 + \gamma_2' \theta_2)]$,	$C_l = CAPE_l/CAPE_0$	
$CAPE = \overline{CAPE} + R[\theta_{eb} - \gamma(\theta_1 + \gamma_2 \theta_2)]$,	$C = CAPE/CAPE_0$	

Table 2 List of variables and convective heating closures for the stochastic multicloud parameterization. $\tilde{\psi}_1(p)$ and $\tilde{\psi}_2(p)$ are the first and second baroclinic heating basis functions. $X^+ \equiv \max(X, 0)$. The constant parameter values are listed in the Table 3.

Variables	Description	Equations
Q_c	Imposed total heating	$Q_c = H_d \cdot \tilde{\psi}_1(p) + (H_c - H_s) \cdot \tilde{\psi}_2(p)$
H_c	Congestus heating	$H_c = \sigma_c \frac{\alpha_c \bar{\alpha}}{H_m} \sqrt{CAPE_l^+}$
H_d	Deep heating	$H_d = \sigma_d \left\{ \overline{Q} + \frac{1}{\overline{\sigma}_d \cdot \tau_{conv}} \left[a_1 \theta_{eb} + a_2 q - a_0(\theta_1 + \gamma_2 \theta_2) \right] \right\}^+$
H_s	SH	$H_s = \sigma_s \alpha_s \left\{ \overline{Q} + \frac{1}{\overline{\sigma}_s \cdot \tau_{conv}} \left[a_1 \theta_{eb} + a_2 q - a_0(\theta_1 + \gamma_2 \theta_2) \right] \right\}^+$
θ_{eb}	Boundary layer equivalent potential temperature	$\frac{\partial \theta_{eb}}{\partial t} + \mathbf{u}(x, y, p_1, t) \cdot \nabla \theta_{eb} = \frac{1}{h} E_s - \frac{1}{h} D$
q	Vertically averaged moisture perturbation	$\frac{\partial q}{\partial t} + \nabla \cdot \left[q(\bar{\mathbf{u}} + \mathbf{u_1} + \tilde{\alpha} \mathbf{u_2}) \right] + \tilde{Q}_1 \nabla \cdot \mathbf{u_1} + \tilde{Q}_2 \nabla \cdot \mathbf{u_2} = -P + \frac{D}{H}$
E_s	Sea surface evaporation	$\frac{1}{h} E_s = \frac{1}{\tau_e} (\theta_{eb}^* - \theta_{eb})$
D	Downdraft mass flux	$D = \frac{m_0}{Q_{R,1}^0} \left\{ Q_{R,1}^0 + \mu(H_s - H_c) \right\}^+ (\theta_{eb} - \theta_{em})$
P	Surface precipitation	$P = \frac{1}{p_B - p_T} \int_{p_T}^{p_B} Q_c(x, y, p, t) dp$

Table 3 List of the default multicloud parameters for SMCM-HOMME. $\overline{X}$ is the prescribed radiative-convective equilibrium (RCE) values of the corresponding variable X.

Parameter	Value	Description
$\tilde{Q}_1$	38.47 K	First baroclinic projection of the background moisture gradient
$\tilde{Q}_2$	38.35 K	Second baroclinic projection of the background moisture gradient
$Q^0_{R,1}$	1K/day	First baroclinic radiative cooling rate
$\bar{\theta}_{eb} - \bar{\theta}_{em}$	11.00K	Discrepancy between θ_{eb} and θ_{em} at RCE
$\bar{\theta}^*_{eb} - \bar{\theta}_{eb}$	10.00K	Discrepancy between saturation and actual θ_{eb} at RCE
a_1/a_2	0.1 / 0.9	Relative contribution of θ_{eb}/q to deep convection
a_0	0.5	Dry convective buoyancy frequency in deep and congestus heating
γ_2/γ_2'	0.25 / 0.6	Relative contribution of θ_2 to deep/congestus heating and to $CAPE/CAPE_l$
μ	0.2	Relative contribution of stratiform and congestus to downdrafts
α_c/α_s	0.25 / 0.5	Congestus/stratiform adjustment coefficient
τ_c/τ_s	1 hr / 3 hrs	Congestus/stratiform adjustment time scale
τ_{conv}	2h	Convective time scale
h	500 m	Prescribed boundary layer height
H	16 km	Average height of the tropical troposphere
$m_0 = \overline{P} \cdot Q^0_{R,1}/[Q^0_{R,1} + \mu(\overline{H}_s - \overline{H}_c)] \cdot 1/(\bar{\theta}_{eb} - \bar{\theta}_{em}) \cdot H$	0.00734 m sec^{-1} (in EXP1)	Scale of downdraft mass flux, value set by RCE solution
$\tau_e = (\theta^*_{eb} - \theta_{eb}) \cdot h/(\overline{P} \cdot H)$	14.8 hrs (in EXP1)	Evaporation time scale, value set by RCE solution
$\tilde{\alpha}$	0.1	Coefficient of second baroclinic velocity component in moisture equation
R	320 J/kg K^{-1}	CAPE constant in Table 1
γ	1.7	Contribution of θ_1 to CAPE anomalies in Table 1
T_0	30 K	Scaling factor of dryness in Table 1
CAPE_0	400 J/kg	Scaling factor of CAPE in Table 1
$n \times n$	1600	Number of lattice sites within each GCM grid box for the stochastic lattice model
τ_{grid}	2	The scaling parameter for cloud transition time scales in Table 1

Table 4 List of the experiments with different warm pool location and SH strength.

Experiment	Location of Warm Pool	SH coefficient (α_s)
EXP1	10^oN	0.50
EXP2	10^oN	0.25
EXP3	10^oN	0.125
EXP4	15^oN	0.50
EXP5	15^oN	0.25
EXP6	15^oN	0.125

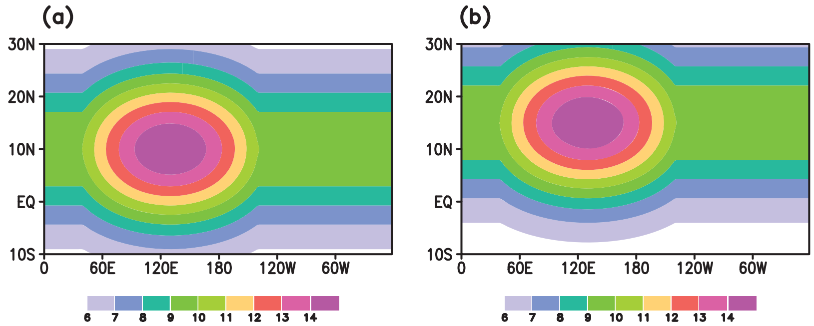

Fig. 1 Structure of the warm pool (K) with center at (a)10°N and (b)15°N for the sensitivity experiments listed in Table 4. Fixed warm pools imply perpetual boreal summer conditions.

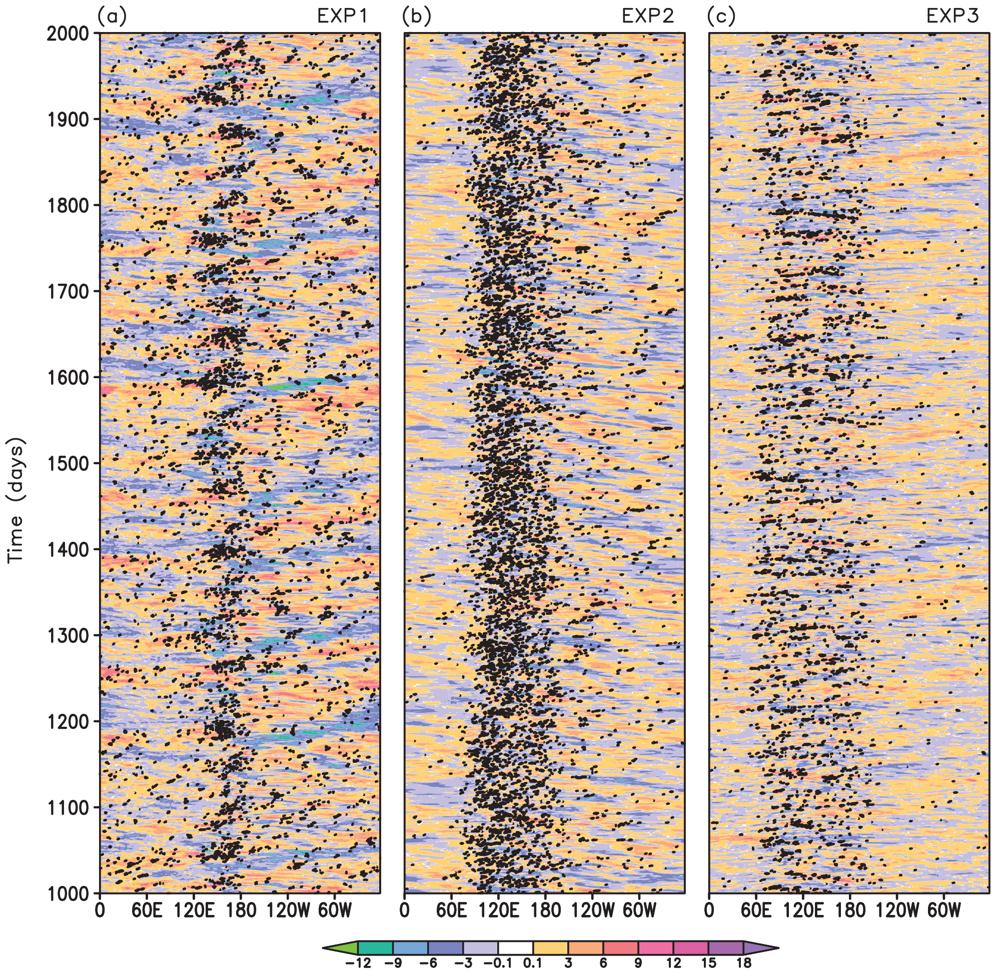

Fig. 2 Longitude-Time plot (Hovmöller diagram) of 850hPa winds (shaded, m s^{-1}) and precipitation anomalies (contour, K day^{-1}) from the last 1000 days of the model simulations averaged over 0°-10°N with varying stratiform fractions, $\alpha_s = 0.5, 0.25, 0.125$ and WPC at 10°N, corresponding to experiments (a) EXP1, (b) EXP2 and (c) EXP3 (See Tab. 4). Starting contour and contour interval of of precipitation is 2 K day^{-1}.

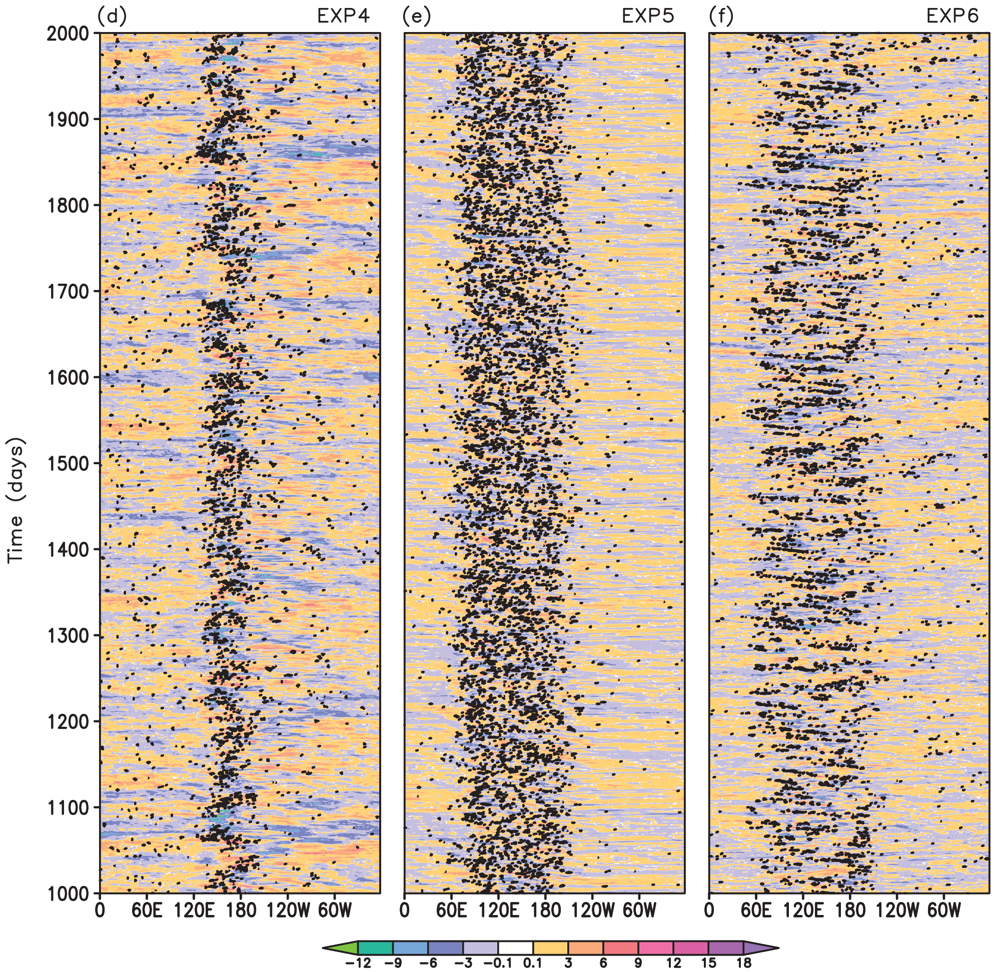

Figure 2 (continued): For (d)EXP4, (e)EXP5 and (f)EXP6, with WPC at 15°N. The data is averaged over 0°-15°N.

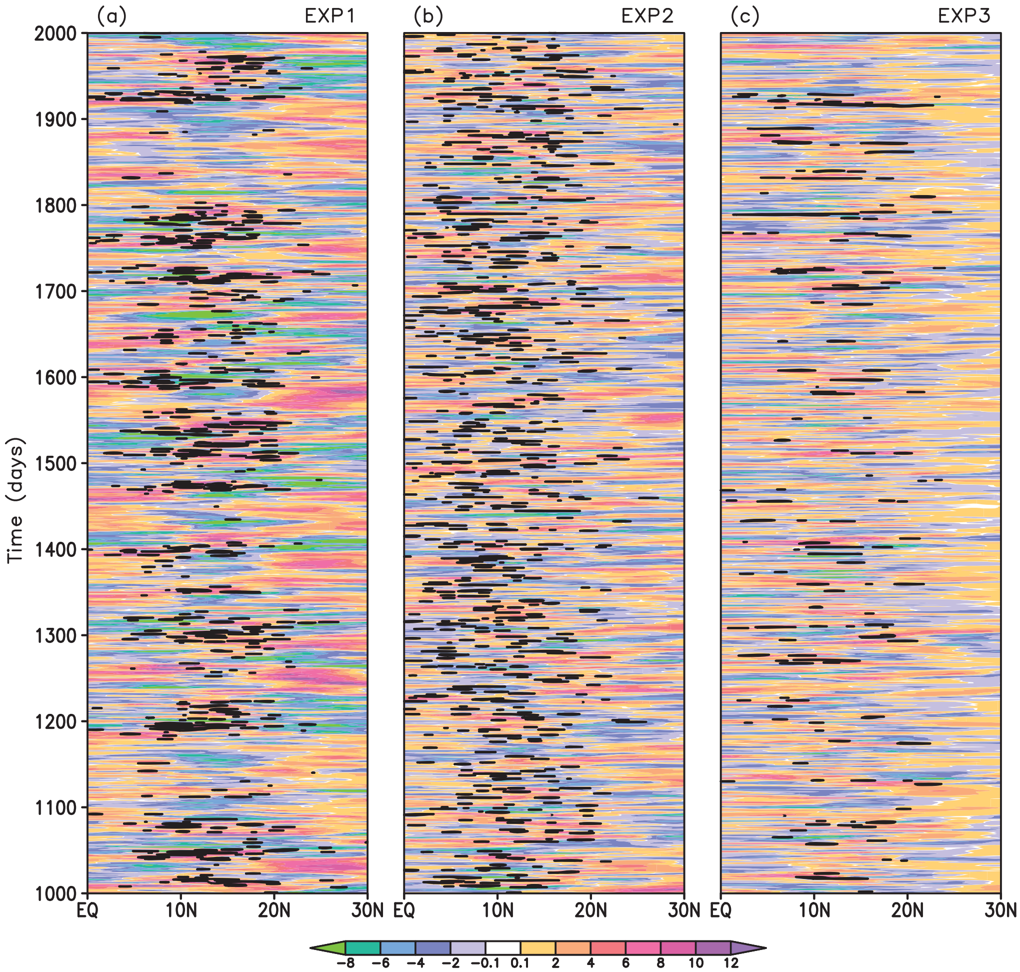

Fig. 3 Latitude-time plot (Hovmöller diagram) of of 850hPa winds (shaded, m s^{-1}) and precipitation anomalies (contour, K day^{-1}) from the last 1000 days of the model simulations averaged over 130°E-150°E with $\alpha_s = 0.5, 0.25, 0.125$. (a)EXP1, (b)EXP2 and (c)EXP3, with WPC at 10°N. Starting contour and contour interval of of precipitation is 3 K day^{-1}.

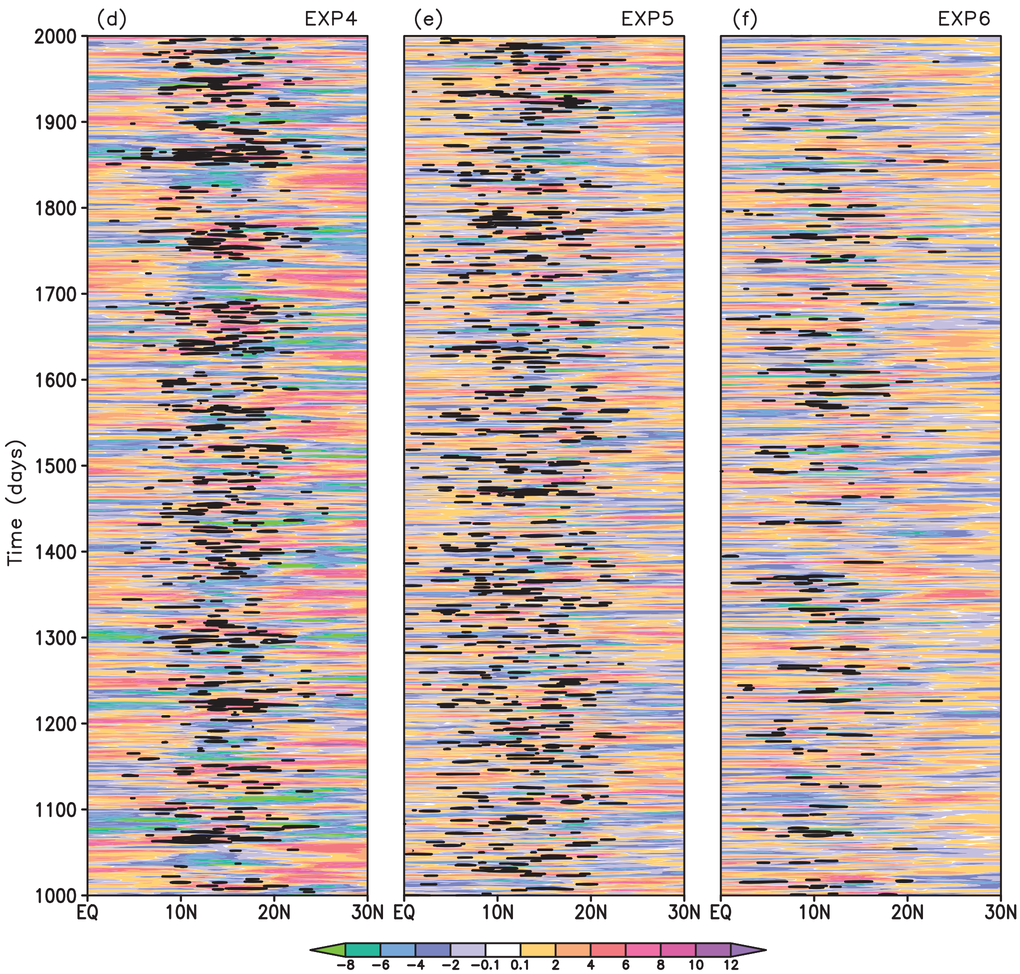

Figure 3 (continued): For (d)EXP4, (e)EXP5 and (f)EXP6, with WPC at 15°N.

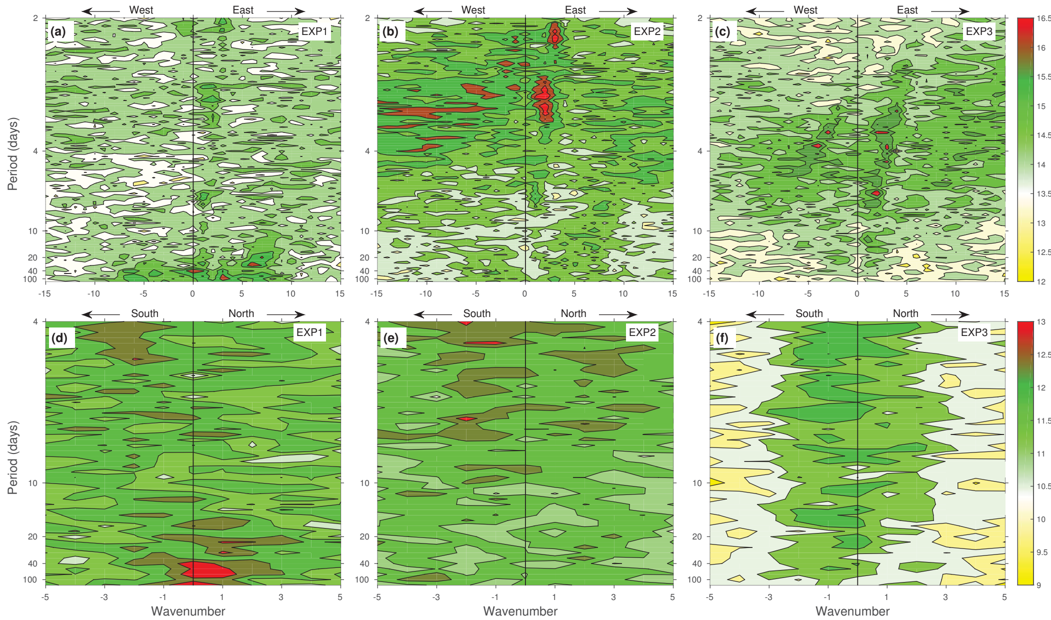

Fig. 4 Log of the spectral power of precipitation for (a,d) EXP1, (b,e) EXP2 and (c,f) EXP3 with the WPC at 10°N. Top panels correspond to East-West Hovmöller plots in Fig. 2 and bottom panels are for the North-South propagation illustrated in Fig. 3.

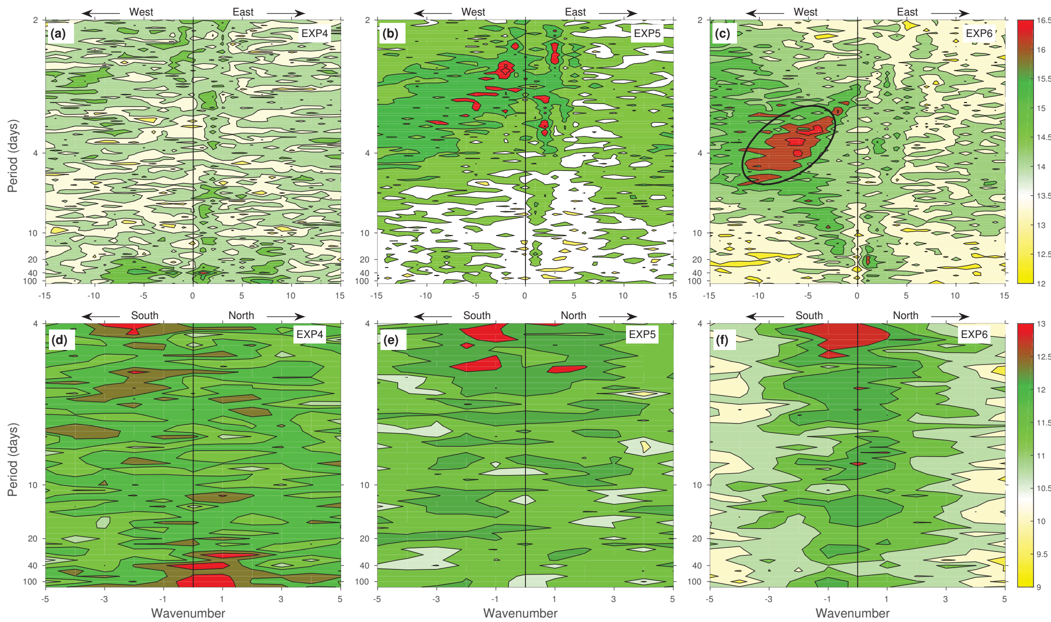

Fig. 5 Same as Fig. 4 but for (a,d)EXP4, (b,e)EXP5 and (c,f)EXP6 with the WPC at 15°N.

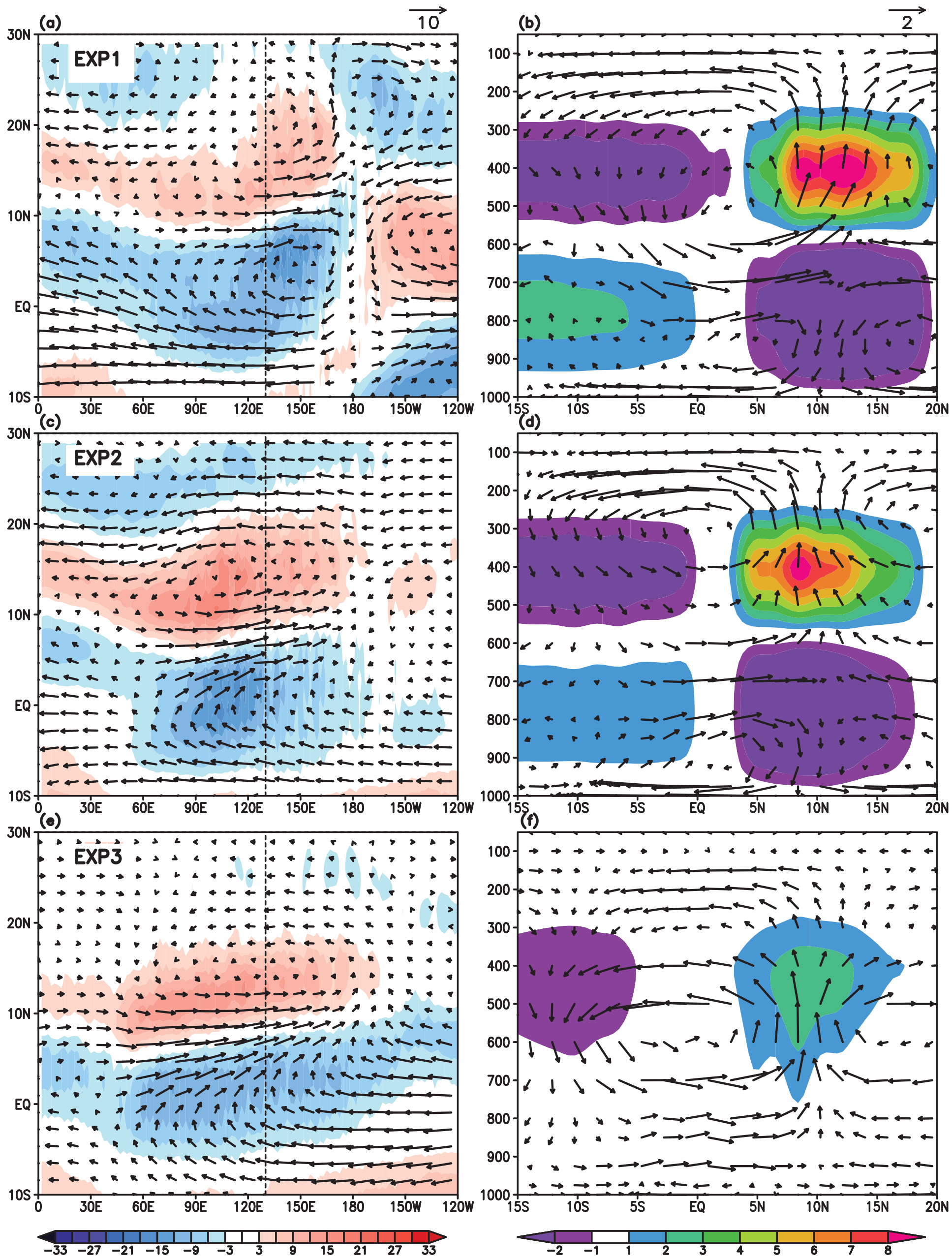

Fig. 6 (a,c,e) Mean 850hPa zonal and meridional winds (arrows, ms^{-1}) and relative vorticity (shaded, $x10^{-6}s^{-1}$) from the sensitivity experiments EXP4, EXP5 and EXP6 respectively. (b,d,f) Mean meridional winds and vertical velocity (arrows, ms^{-1}) and total heating (QHe; $K.day^{-1}$) averaged over 60°E-180°E from EXP4, EXP5 and EXP6 simulations respectively. Mean is calculated from the last 1000 days of simulation. The vertical dotted line indicate the longitude of the WPC.

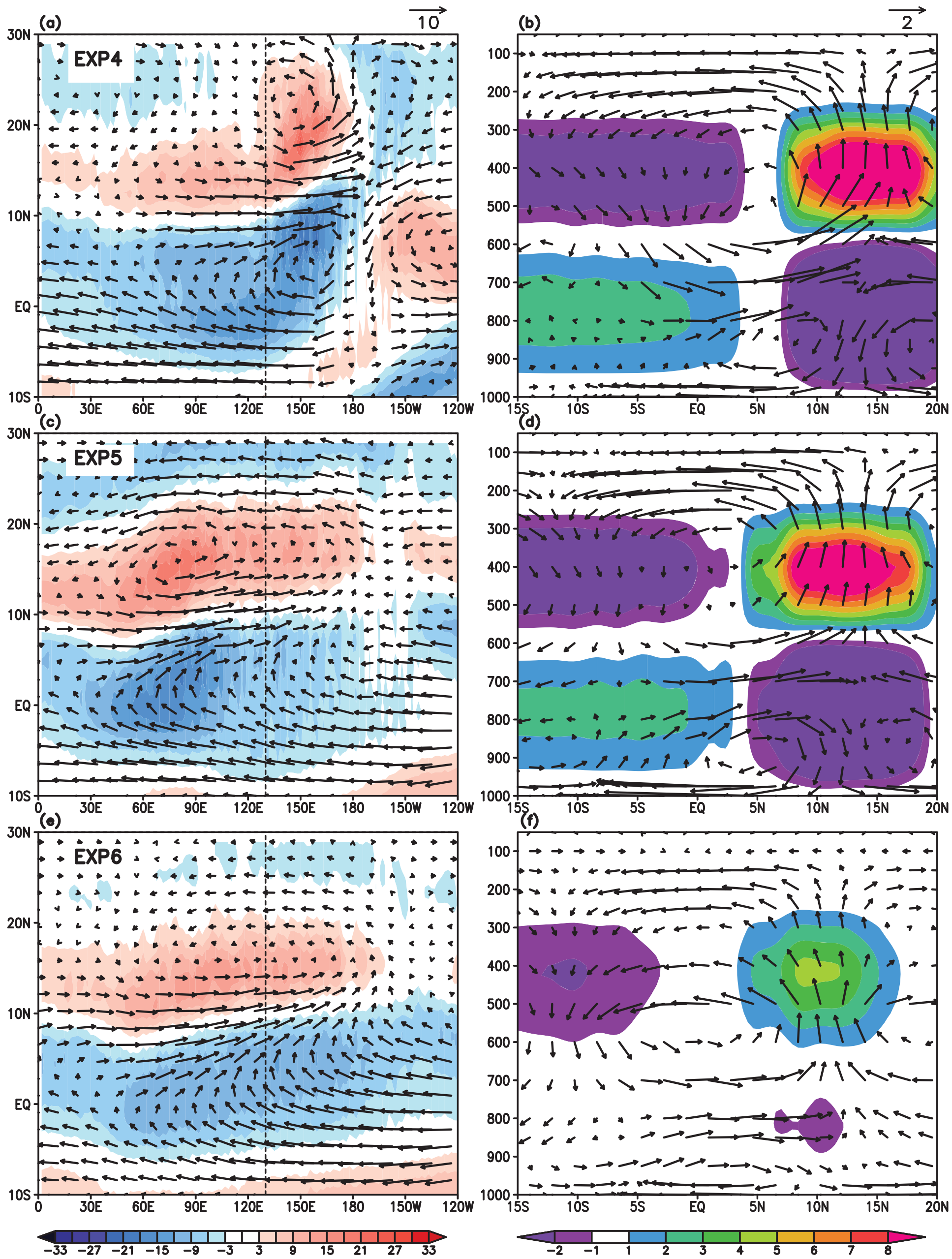

Fig. 7 Same as Figure 6 but for (a,b) EXP4, (c,d) EXP5 and (e,f) EXP6 with the WPC at 15°N.

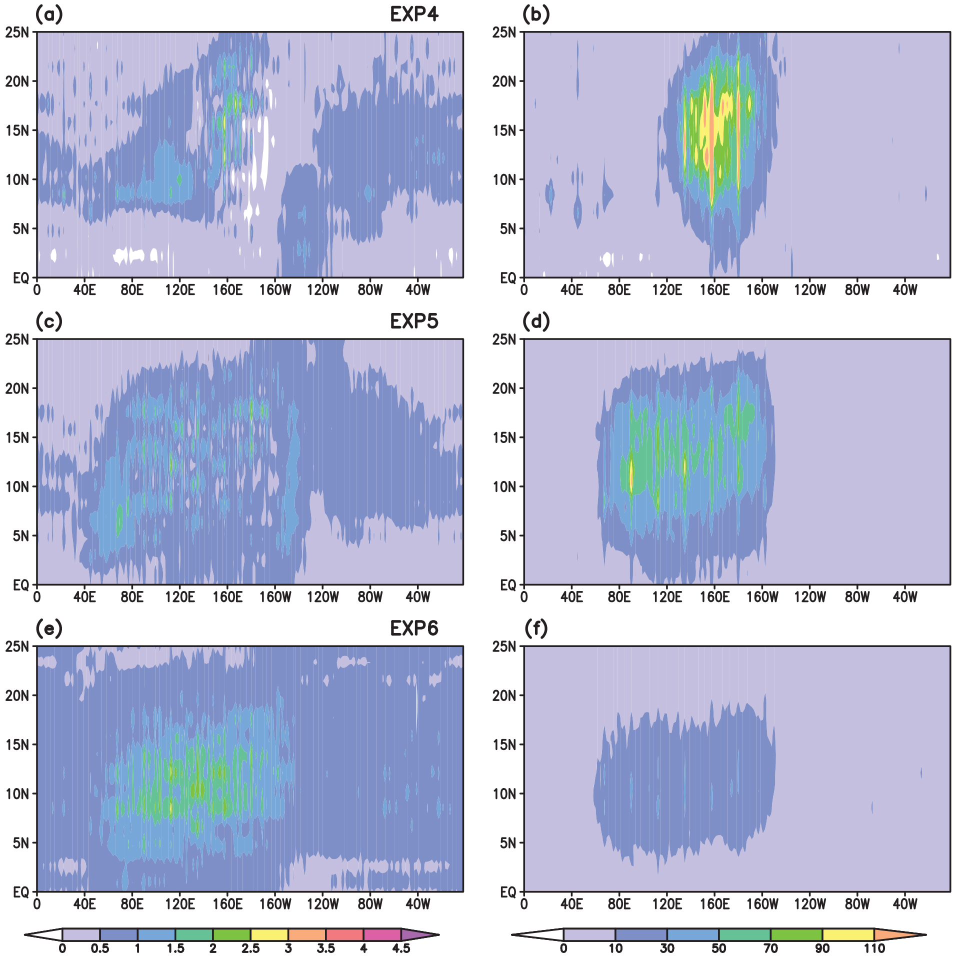

Fig. 8 Mean (left) and variance (right) of precipitation for (a,b) EXP4, (c,d) EXP5 and (e,f) EXP6 with WPC at 15°N, corresponding to the last 1000 days of simulation.

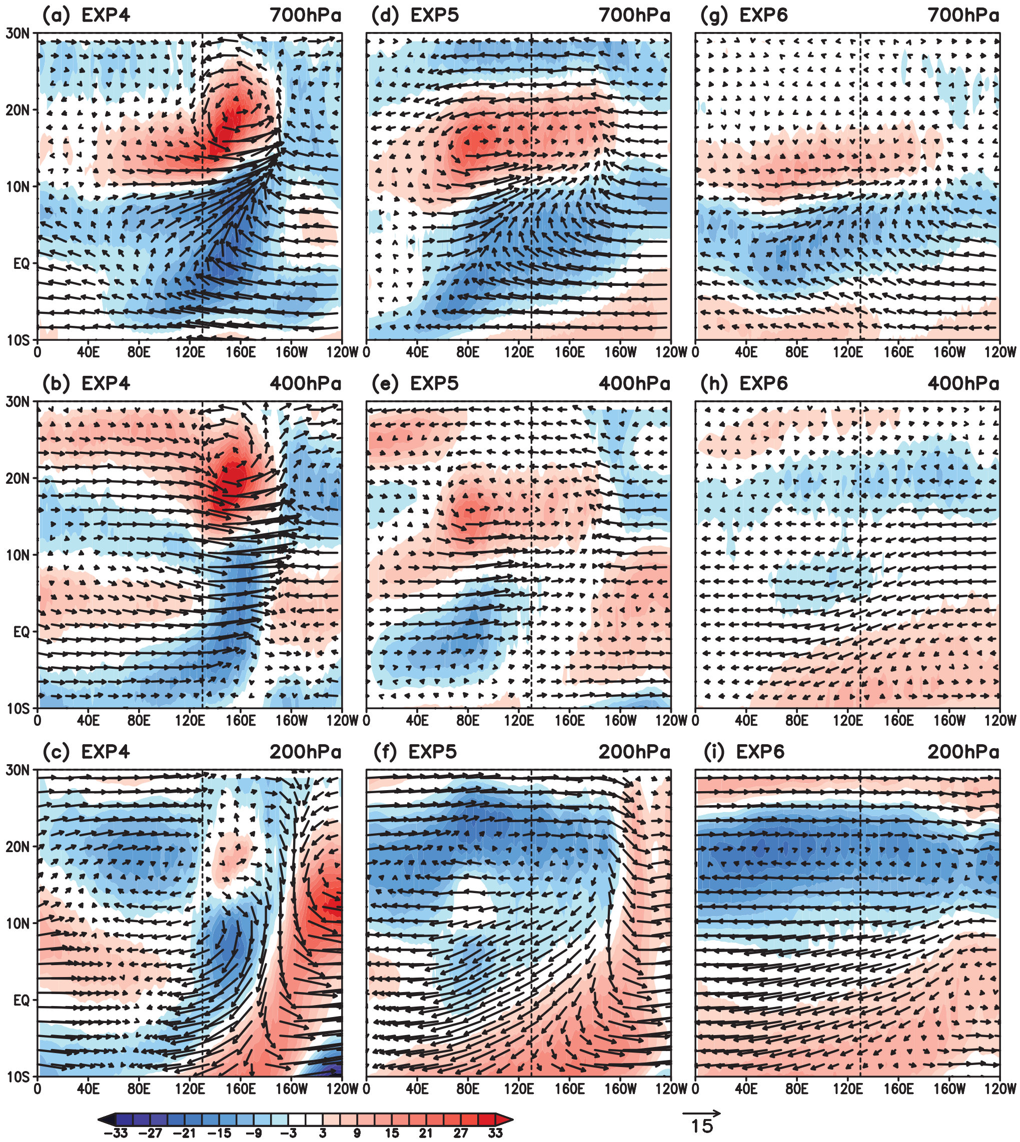

Fig. 9 Horizontal slices of time mean vorticity (shaded,x$10^{-6}s^{-1}$)) overlaid with horizontal wind vectors (arrows, ms^{-1}) at various heights demonstrating the variation in MT depth with respect to the stratiform fraction parameter for the cases with WPC at 15°N: (a,b,c) EXP4, (d,e,f) EXP5 and (g,h,i) EXP6. The dashed line indicates the longitude of the WPC.

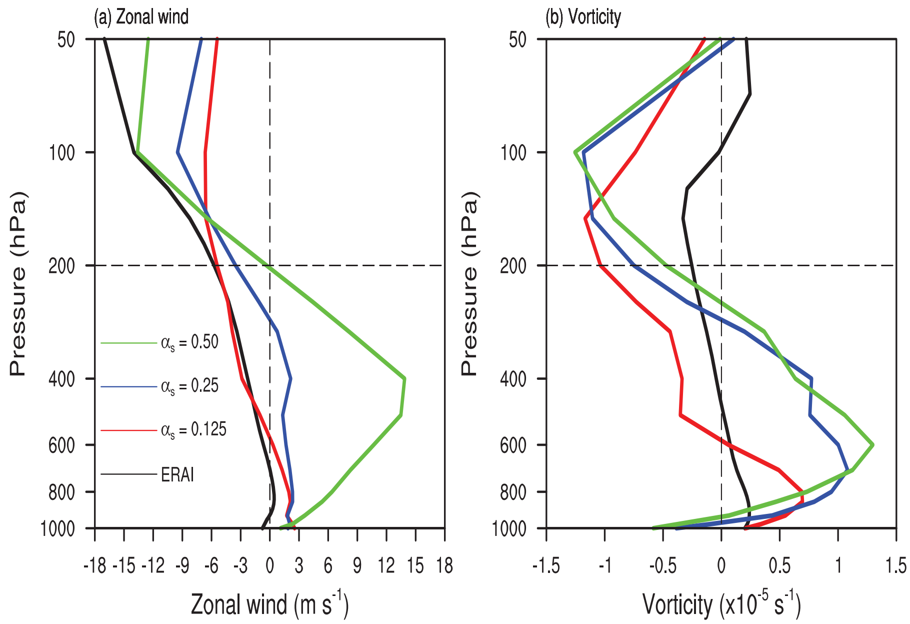

Fig. 10 Mean zonal wind (a) and vorticity (b) profiles, averaged in time over the last 1000 days and horizontally over the box 10°N–20°N and 80°E–180°E, associated with the three different stratiform fraction, for the cases with WPC at 15°N (EXP4:green, EXP5:blue, EXP6:red) and the corresponding climatological reference profiles obtained from the ERA Interim reanalysis data (black). The horizontal and vertical dashed lines denote the hight above which the heating profiles are set to zero (see Khouider et al (2011); Deng et al (2015a) for details) and the absolute zero reference, respectively.

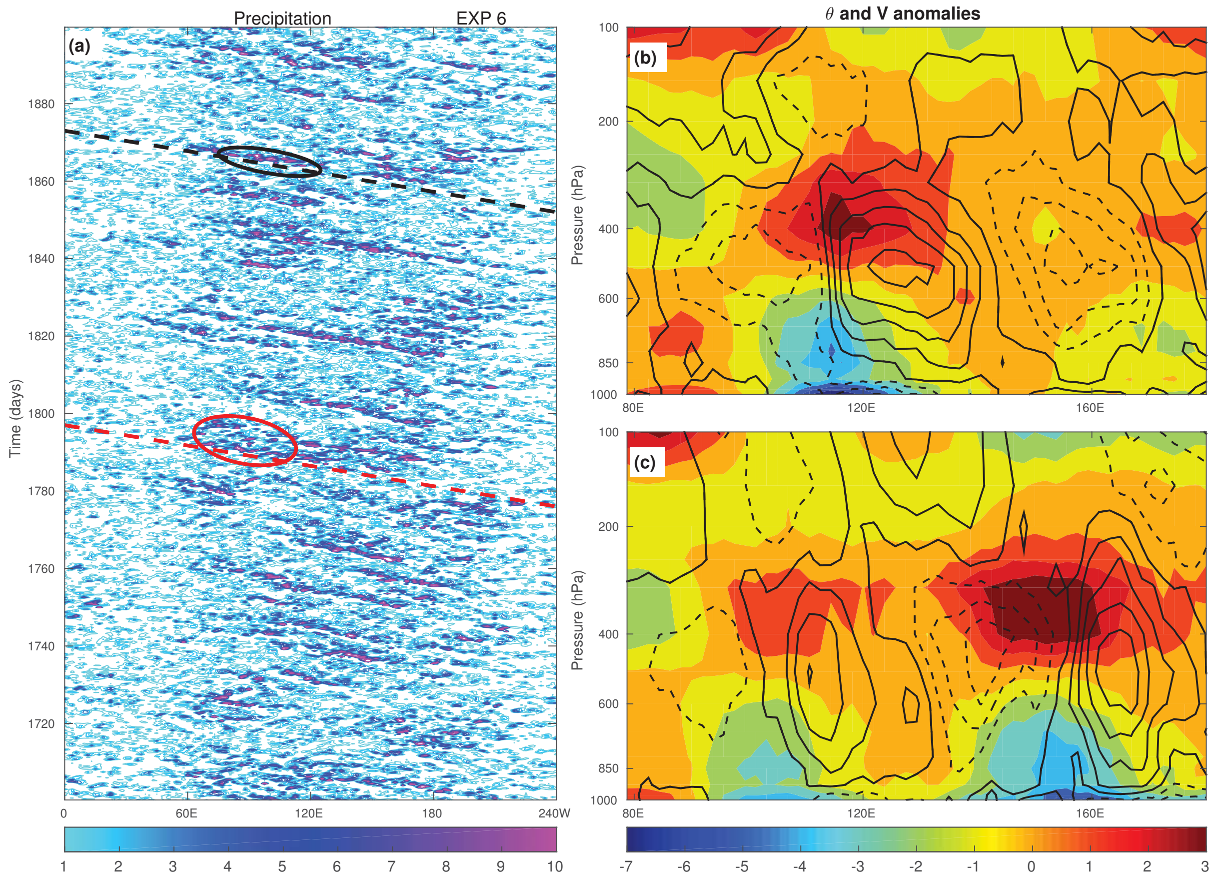

Fig. 11 (a) Closeup of the Hovmöller of precipitation (K day^{-1}) between 1700 days and 1800 days showcasing the persistence of westward moving disturbances. The dashed lines mark a westward speed about 19.3 m s^{-1}. (b and c) Vertical structure composites of meridional winds (contours, negative dashed, contour interval: 2 m s^{-1}) and potential temperature anomalies (colors, K) corresponding to the two events (marked, respectively, by the black and red circles) of the associated low pressure systems, for case with WPC at 15°N and $\alpha_s = 0.125$ (EXP 6). Note that the red event (c) consists of a packet of two waves. The anomalies are averaged in the 8-day moving window roughly along (b) the black dashed line starting at day 1865 and (c) the red dashed line starting at day 1790.